Elastostatic modeling and shape optimization of a 6-dof haptic interface device

Stéphane Caro, Damien Chablat, Chao Chen

ELASTOSTATIC MODELING AND SHAPE OPTIMIZATION OF A 6-DOF HAPTIC INTERFACE DEVICE

Stéphane CARO[†], **Damien CHABLAT**[†], **Chao CHEN**[⋆]
† Institut de Recherche en Communications et Cybernétique de Nantes
UMR CNRS n° 6597
1 rue de la Noë, 44321 Nantes, France
⋆ Department of Mechanical and Aerospace Engineering, Monash University, Australia
Email: {caro, chablat}@irccyn.ec-nantes.fr, chao.chen@monash.edu

ABSTRACT

This paper deals with the shape optimization of a six degree-of-freedom haptic interface device. This six-dof epicyclic-parallel manipulator has all actuators located on the ground. A regular dexterous workspace is introduced to represent the mobility of user's hand. Throughout this workspace, the deviation of the mobile platform is bounded to provide a better feeling to the user and the masses in motion are minimized to increase the transparency of the haptic device. The stiffness model is written using a virtual joint method and compared with the results obtained with the finite element analysis to be validated. Finally, the shape of the links are optimized in order to minimize the masses in motion while guaranteeing a given stiffness throughout the regular workspace of the mechanism.

INTRODUCTION

There is a large number of parallel manipulators, which have been reported over the past three decades. They can be divided into three-dof, four-dof, five-dof and six-dof parallel manipulators [1–4]. In three-dof parallel manipulators, there are three-dof translational parallel manipulators [5–7], three-dof rotational parallel manipulators [8, 9] and three-dof parallel manipulators with mixed (translational and rotational) motion capabilities [10, 11]. Among the four-dof parallel manipulators, examples include the four-dof four-URU parallel mechanism [12] and the Schönflies-motion generator [13]. There are also five-dof parallel manipulators, such as the 3T2R parallel manipulators [14–16]. For six-dof manipulators, the number of all possible architectures can be extremely large [17]. Six-legged six-dof parallel manipulators, such as the Gough-Stewart platform, have high stiffness and accuracy but suffer from a small workspace and limb interference. Three-legged six-dof manipulators were introduced to overcome this workspace limitation and do not suffer from the same limb interference as their six-legged counterparts [18]. However, to achieve six-dof with only three legs requires actuators to be mounted on the moving limbs, thus increasing the mass and inertia of the moving parts. Three-legged manipulators have been reported, such as [19–24]. However, very few of them have all actuators allocated on the ground, [21, 24] being some examples. A differential drive system is used in [21] to allow for all actuators to be mounted on the base whereas [24] use a gimbal mechanism.

This paper deals with the shape optimization of a six-dof three-legged parallel manipulator with all actuators mounted to the base, called the Monash Epicyclic-Parallel Manipulator (MEPaM) [25, 26]. The design is achieved by taking advantages of two-dof planetary belt systems. By mounting actuators on the base, the mass and inertia of the moving links is greatly reduced resulting in a lightweight six-dof parallel manipulator. The shape of the links are optimized in order to minimize the masses in motion while guaranteeing a given stiffness throughout a regular workspace of the mechanism. The displacement of the mobile platform due to external loading is limited to be compatible with the user's perception.

The paper is organized as follows. First, a prototype of the MEPaM is presented. Then, its elastostatic model is obtained by using the Virtual Joint method (VJM) introduced in [27, 28] and validated with the structural analysis workbench of CATIA commercial software. Finally, the shape optimization of the manipulator is performed and the results are discussed.

MECHANISM UNDER STUDY

A prototype of the MEPaM is shown in Fig. 1. The moving platform has six degree-of-freedom with two actuated joints in each leg. The revolute joints are driven by belt connected to the actuators mounted to the base of each leg. Links 2 and 3 are connected with a cylindrical joint and Link 3 is connected to the moving platform through passive universal joint.

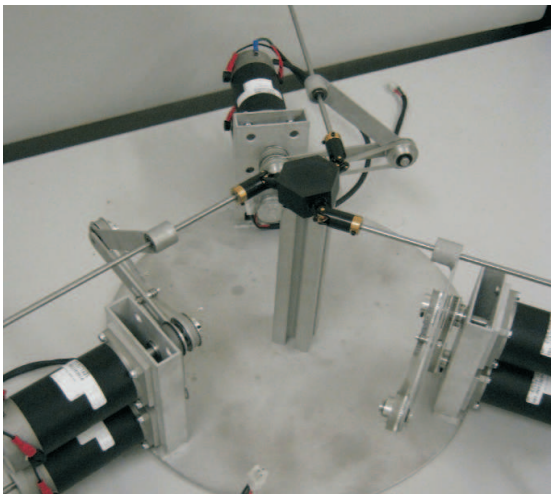

Figure 1. A prototype of the MEPaM

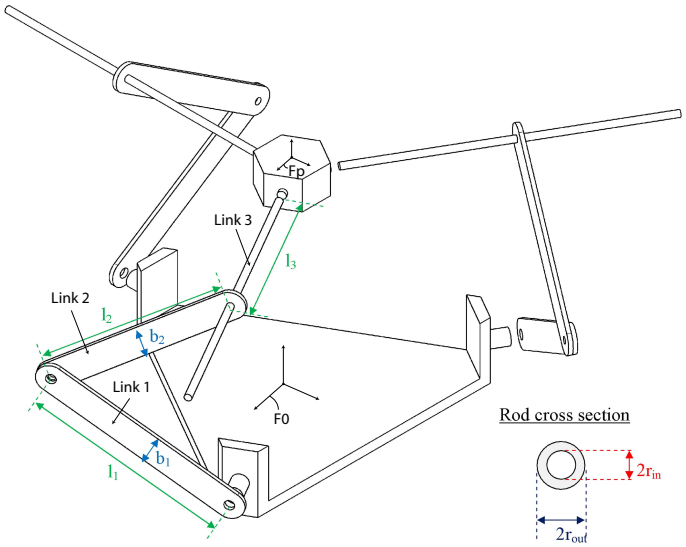

Figure 2. Simplified model of the MEPaM

In the scope of this paper, the planetary belt systems are supposed to be replaced by direct actuation systems and the ball bearings located at the cylindrical joints are not considered in the model. The simplified model of the mechanism is shown in Fig. 2. $\mathcal{F}_0$ and $\mathcal{F}_P$ denote the base frame and the moving-platform frame, respectively. The geometric parameters of the MEPaM are given in Table 1.

Table 1. Geometric parameters of the MEPaM

Links 1 & 2	$l = 0.1375$ m	Link 3	$r_{out} = 0.0025$ m
	$b = 0.0200$ m		
	$h = 0.0030$ m		
Base	$r_b = 0.1450$ m	Platform	$r_p = 0.0275$ m

ELASTOSTATIC MODELING OF THE MEPaM

Stiffness model with a virtual joint method

The virtual joint method used to derive the Cartesian stiffness matrix of the manipulator under study and the notations used in this section are explained in [28]. The *control loop stiffness* $k^i_{(a1,\,a2)}$ associated with the two actuators of the ith leg and the links' deflections are considered while defining the stiffness model of the MEPaM. The former are defined as follows:

$$k^i_{(a1,\,a2)} = 1 \times 10^8 \; N.rad^{-1} \tag{1}$$

The actuated joint stiffness is supposed to be high enough in order to focus mainly on the effect of the links's flexibility on the overall manipulator stiffness. The first and the second links of each leg are supposed to be axi-symmetrical about the x-axis of their local frame. Hence, the inverse of their stiffness matrix is expressed as:

$$[\mathbf{K}^i_{1,2}]^{-1} = \begin{bmatrix} \frac{l^3_{1,2}}{3EI_{(1,2)x}} & 0 & 0 & 0 & 0 & 0 \\ 0 & \frac{l^3_{1,2}}{3EI_{(1,2)z}} & 0 & 0 & 0 & \frac{l^2_{1,2}}{2EI_{(1,2)z}} \\ 0 & 0 & \frac{l^3_{1,2}}{3EI_{(1,2)y}} & 0 & -\frac{l^2_{1,2}}{2EI_{(1,2)y}} & 0 \\ 0 & 0 & 0 & \frac{l_{1,2}}{GJ_{(1,2)}} & 0 & 0 \\ 0 & 0 & -\frac{l^2_{1,2}}{2EI_{(1,2)y}} & 0 & \frac{l_{1,2}}{EI_{(1,2)y}} & 0 \\ 0 & \frac{l^2_{1,2}}{2EI_{(1,2)z}} & 0 & 0 & 0 & \frac{l_{1,2}}{EI_{(1,2)z}} \end{bmatrix}^{-1} \tag{2}$$

Likewise, the third link of each leg is supposed to be axi-symmetrical about the z-axis of its local frame. Hence, the in-

verse of its stiffness matrix is expressed as:

$$[\mathbf{K}_3^i]^{-1} = \begin{bmatrix} \frac{r_1^3}{3EI_{3y}} & 0 & 0 & 0 & \frac{r_1^2}{2EI_{3y}} & 0 \\ 0 & \frac{r_1^3}{3EI_{3x}} & 0 & -\frac{r_1^2}{2EI_{3x}} & 0 & 0 \\ 0 & 0 & \frac{r_1^3}{3EI_{3z}} & 0 & 0 & 0 \\ 0 & -\frac{r_1^2}{2EI_{3x}} & 0 & \frac{r_1}{2EI_{3x}} & 0 & 0 \\ \frac{r_1^2}{2EI_{3y}} & 0 & 0 & 0 & \frac{r_1}{EI_{3y}} & 0 \\ 0 & 0 & 0 & 0 & 0 & \frac{r_1}{GJ_3} \end{bmatrix}^{-1} \quad (3)$$

The links are supposed to be made up of stainless steel. Therefore, the Young's modulus E is equal to 210×10^6 MPa and the Poisson's ratio is equal to 0.3. I_{ix}, I_{iy}, and I_{iz} are the area moment of inertia and J_i is the torsion moment of the ith link. From Eqs. (1) to (3), the aggregated spring stiffness matrix associated with the ith leg of the MEPaM takes the form:

$$\mathbf{K}_\theta^i = \text{diag}\left(k_{a1}^i, \mathbf{K}_1^i, k_{a2}^i, \mathbf{K}_2^i, \mathbf{K}_3^i\right) \quad (4)$$

Hence, the Cartesian stiffness matrix defining the motion-to-force mapping associated with the ith leg of the MEPaM is obtained by solving the following equation:

$$\begin{bmatrix} \mathbf{S}_\theta^i & \mathbf{J}_q^i \\ \mathbf{J}_q^{i\top} & \mathbf{0} \end{bmatrix} \begin{bmatrix} \mathbf{f}^i \\ \delta\mathbf{q}^i \end{bmatrix} = \begin{bmatrix} \delta\mathbf{x}^i \\ \mathbf{0} \end{bmatrix} \quad (5)$$

where $\mathbf{S}_\theta^i = \mathbf{J}_\theta^i [\mathbf{K}_\theta^i]^{-1} \mathbf{J}_\theta^{i\top}$. The inverse of the first left-hand side matrix gives the Cartesian stiffness of the kinematic chain, $\mathbf{K}_C^i$ where the 6×6 matrix is extracted from the top left hand corner of the inverse matrix.

Once the Cartesian stiffness matrices $\mathbf{K}_C^i$, $i = 1, \ldots, 3$, for the three kinematic chains are computed, the Cartesian stiffness matrix of the MEPaM can be found by simple addition, namely,

$$\mathbf{K}_{MEPaM} = \sum_{i=1}^{3} \mathbf{K}_C^i \quad (6)$$

It is noteworthy that this model only stands for unloaded modes and assumes a linearization of displacement around the equilibrium position. A more advanced model is described in [29], but is more time consuming as the external loads are performed iteratively.

CAD and FEA modeling

A Computer Aided Design (CAD) model of the MEPaM manipulator was built under CATIA commercial software. For the Finite Element Analysis (FEA), the components of the MEPaM are designed individually and the manipulator is assembled as shown in Fig. 3. Rigid virtual joints, represented by some red lines in Fig. 3, are used to connect all the components. The benefit of using rigid virtual joints connection is that the users can define the joint stiffness in their desired directions.

Then, the actuator stiffness is defined by connection properties between the rigid virtual joints. A slider connection property is introduced for the cylindrical joint that connects link 2 to link 3. This connection property enables link 3 to slide freely inside the connection hole of link 2.

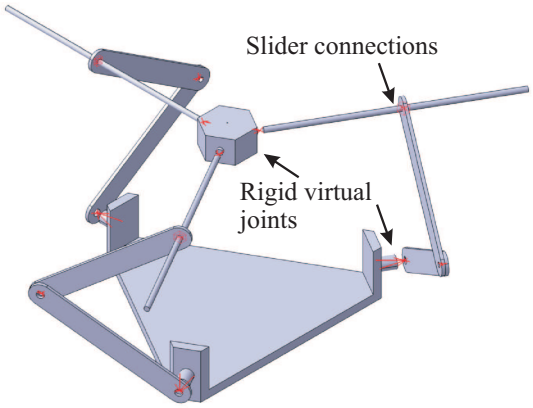

Figure 3. FEA assembly model of the MEPaM under CATIA

Stiffness of the MEPaM throughout its regular workspace

The VJM and FEA models are simulated with three individual forces and three individual moments applied on the moving platform for six different locations within the workspace. The magnitudes of the corresponding force and moments are equal to 10 N and 0.5 Nm, respectively. The 2-norm of the point-displacement screw, $\|\delta\mathbf{p}\|_2$, of the moving-platform and the 2-norm of its orientation vector, $\|\delta\phi\|_2$, are defined as:

$$\|\delta\mathbf{p}\|_2 = \sqrt{\delta p_x^2 + \delta p_y^2 + \delta p_z^2} \quad (7)$$

$$\|\delta\phi\|_2 = \sqrt{\delta\varphi_x^2 + \delta\varphi_y^2 + \delta\varphi_z^2} \quad (8)$$

Thanks to the symmetry of the MEPaM, a cylindrical regular workspace is defined and shown in Fig. 4. Its diameter is equal to 170 mm and the Z-coordinate of the geometric center of the moving platform varies between 50 mm and 250 mm in the base frame. This regular workspace turns to be similar to the workspace of the Virtuose 6D Desktop from Haption [30].

Figures 5 to 10 illustrate the isocontours of the linear and angular displacements of the moving-platform throughout the cylindrical regular workspace of the MEPaM for different wrenches applied on the moving-platform, namely, $F_x = 10$ N, $F_y = 10$ N, $F_z = 10$ N, $M_x = 0.5$ N.m, $M_y = 0.5$ N.m and $M_z = 0.5$ N.m, respectively. It is apparent that the largest displacements occur at the border of the positional regular workspace. The point-displacement of the moving-platform is a maximum

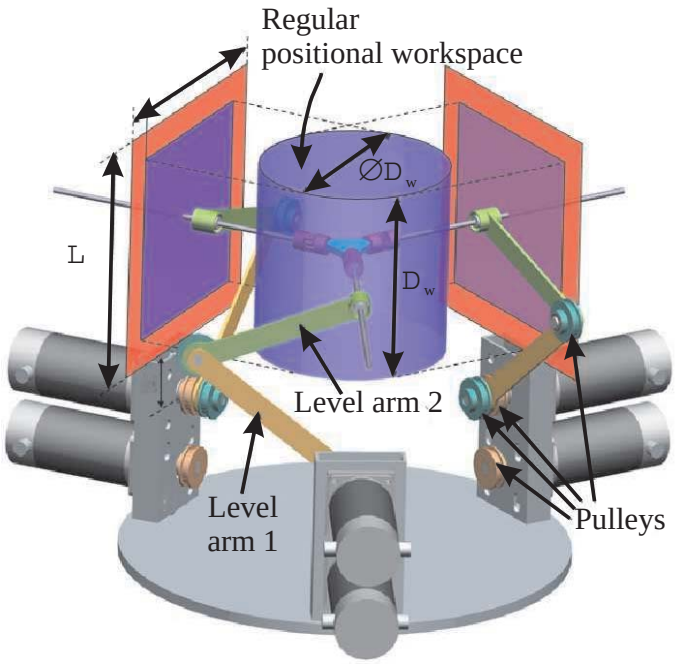

Figure 4. Positional regular workspace of the MEPaM

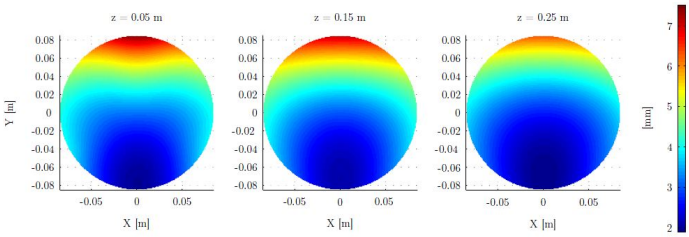

(a) $\|\delta\mathbf{p}\|_2$, $F_x = 10$ N

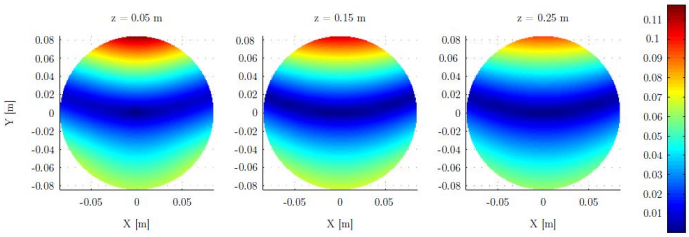

(b) $\|\delta\phi\|_2$ (rad), $F_x = 10$ N

Figure 5. Linear and angular displacement of the moving-platform throughout the cylindrical regular workspace for $F_x = 10$ N

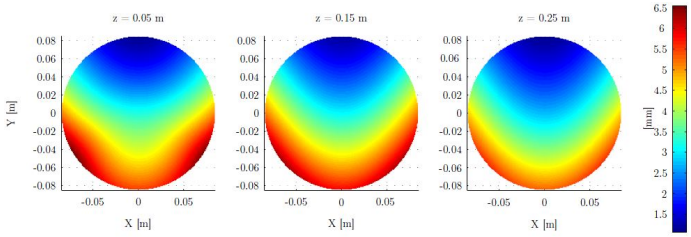

(a) $\|\delta\mathbf{p}\|_2$, $F_y = 10$ N

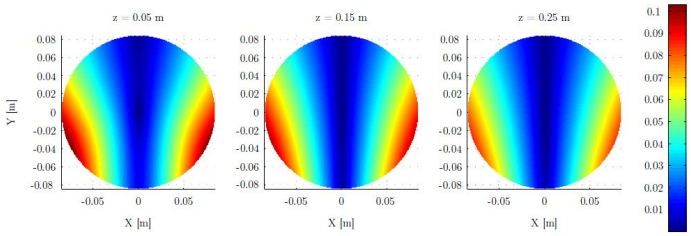

(b) $\|\delta\phi\|_2$ (rad), $F_y = 10$ N

Figure 6. Linear and angular displacement of the moving-platform throughout the cylindrical regular workspace for $F_y = 10$ N

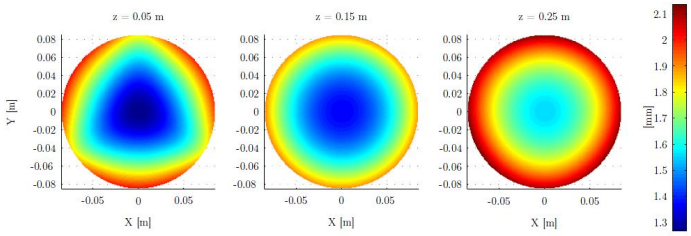

(a) $\|\delta\mathbf{p}\|_2$, $F_z = 10$ N

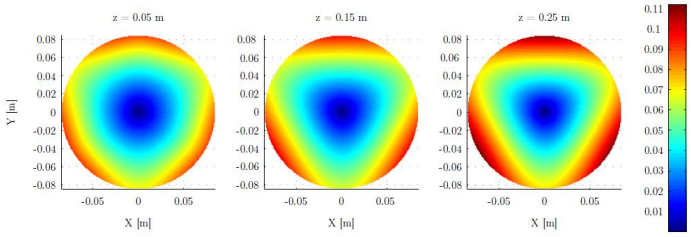

(b) $\|\delta\phi\|_2$ (rad), $F_z = 10$ N

Figure 7. Linear and angular displacement of the moving-platform throughout the cylindrical regular workspace for $F_z = 10$ N

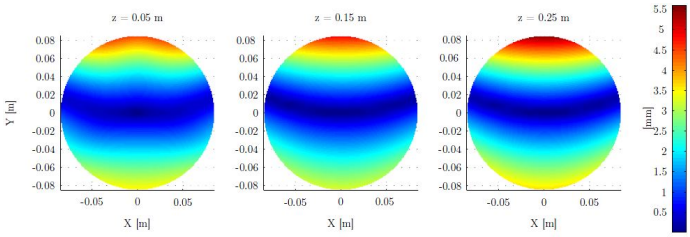

(a) $\|\delta \mathbf{p}\|_2$, $M_x = 0.5$ N.m

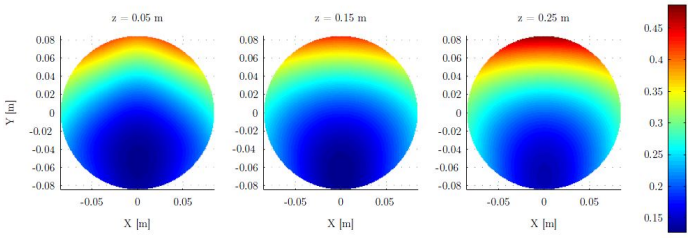

(b) $\|\delta \phi\|_2$ (rad), $M_x = 0.5$ N.m

Figure 8. Linear and angular displacement of the moving-platform throughout the cylindrical regular workspace for $M_x = 0.5$ N.m

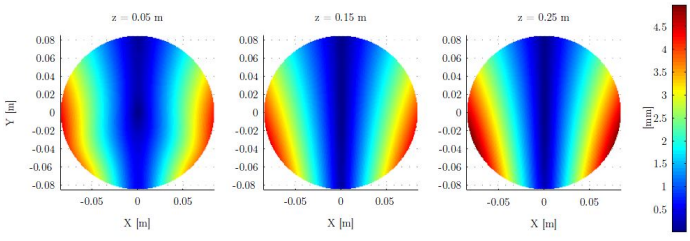

(a) $\|\delta \mathbf{p}\|_2$, $M_y = 0.5$ N.m

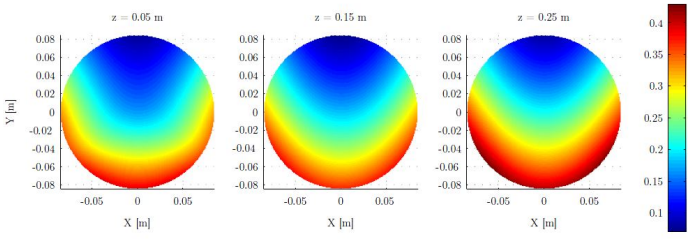

(b) $\|\delta \phi\|_2$ (rad), $M_y = 0.5$ N.m

Figure 9. Linear and angular displacement of the moving-platform throughout the cylindrical regular workspace for $M_y = 0.5$ N.m

and equal to 7 mm for $F_x = 10$ N, $x = 0$ mm, $y = 80$ mm and $z = 50$ mm. The angular displacement of the moving-platform is a maximum and equal to 0.48 rad for $M_x = 0.5$ N.m, $x = 0$ mm, $y = 80$ mm and $z = 250$ mm.

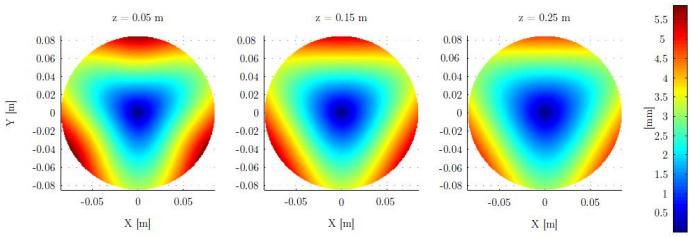

(a) $\|\delta \mathbf{p}\|_2$, $M_z = 0.5$ N.m

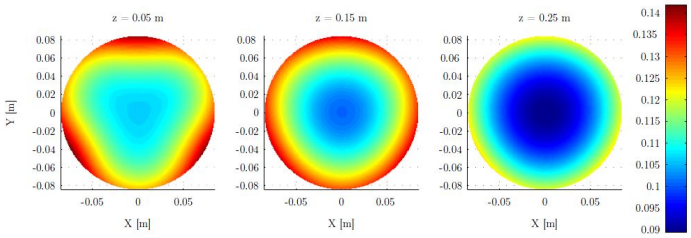

(b) $\|\delta \phi\|_2$ (rad), $M_z = 0.5$ N.m

Figure 10. Linear and angular displacement of the moving-platform throughout the cylindrical regular workspace for $M_z = 0.5$ N.m

Comparison between VJM model and FEA model

The VJM model described is computed with MATLAB computational software. In general, the difference between the results obtained with the VJM model and those obtained with the CAD model are below 10%. At the center of the working plane, it appears that the difference between the two models in terms of rotation angle is relatively high. The same phenomenon appears for the linear displacement of the moving platform when some torques are applied on the latter. To explain the phenomenon, it is necessary to understand the moving platform's displacement corresponding to the stiffness of the leg of the manipulator. Due to the leg configuration, all the legs of the manipulator have different stiffness in different directions. The stiffness differences amongst the legs resulted the moving platform to translate a small distance and to rotate in a small angle when forces or torques are applied. All the legs of the manipulator are connected to the moving platform through a passive universal joint. The passive universal joint allows the moving platform to rotate freely. The differences in leg stiffness and passive universal joint affect the translation and rotation of the moving platform. Accordingly, the results obtained with the VJM model and those obtained with the CAD model differ slightly for some poses of the moving-platform because of the different modelings of the passive universal joints in the two models. Nevertheless, we can claim that the VJM model of the MEPaM provides a good approximation of its real stiffness throughout the regular workspace.

OPTIMIZATION PROBLEM

Objective function

The stiffness of the MEPaM depends on its configuration and the dimensions of its components. The relation between the MEPaM stiffness and its configuration is characterized by Eq. (6). This section aims at defining the optimum shape of the MEPaM's components in order to minimize the mass of the components in motion while satisfying a given stiffness throughout the regular workspace of the manipulator. Therefore, the objective function of the optimization problem is the mass m_{MEPaM} of the MEPaM and is defined as follows:

$$m_{MEPaM} = f_1(\mathbf{x}, \mathbf{q}) \rightarrow min \tag{9}$$

where vector $\mathbf{x}$ contains the decision variables of the optimization problem at hand. Vector $\mathbf{q}$ is composed of the parameters of the optimization problem at hand, namely, the Young's modulus E, the Poisson's ratio μ and the density ρ of the material and the link lengths.

Decision variables

Figure 11 represents the possible cross section types for the links of the MEPaM. On the one hand, the first two links of each leg are supposed to be composed of a rectangular hollow, a I-shaped or a H-shaped cross section type. On the other hand, the cross section of the third link is assumed to be circular hollow to realize the cylindrical joint between link 2 and link 3. As shown in Fig. 11, the rectangular hollow, I-shaped or a H-shaped cross section types are characterized by design variables b, h, s and t. The circular hollow cross section is parameterized by its inner and outer radii r_{in} and r_{out}, respectively.

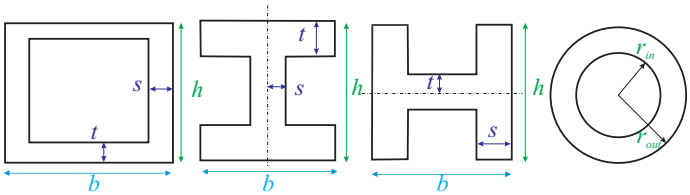

Figure 11. Possible cross-section types for the links

Moreover, the architecture of the MEPaM is supposed to be symmetrical, namely, its three legs are the same.

As a result, the decision variable vector $\mathbf{x}$ takes the form:

$$\mathbf{x} = \left[k_1 \; b_1 \; h_1 \; s_1 \; t_1 \; k_2 \; b_2 \; h_2 \; s_2 \; t_2 \; r_{in} \; r_{out} \right]^T \tag{10}$$

where b_i, h_i, s_i, t_i characterize the dimensions of the cross section of the ith link, $i = 1, 2$, while k_i denotes its cross section type, namely,

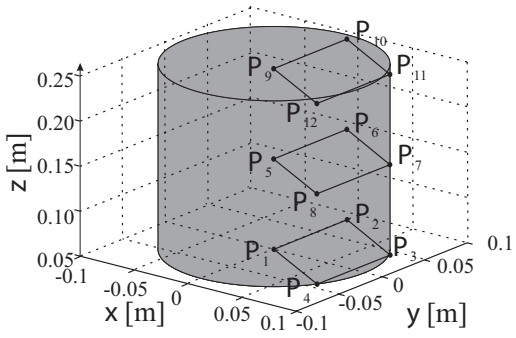

Figure 12. Location of the sampling points within the regular workspace

- $k_i = 1$ stands for a rectangular hollow cross section type;
- $k_i = 2$ stands for a I-shaped cross section type;
- $k_i = 3$ stands for a H-shaped cross section type.

r_{in} and r_{out} are the inner and outer radii of the circular hollow section of the third link.

Constraints

The constraints of the optimization problem at hand are related to the feasibility of the cross sections and the maximum point- and angular displacements of the moving-platform allowed for a given wrench applied on the latter.

As a matter of fact, the maximum point-displacement of the moving-platform allowed for a force of 10 N applied on the latter is equal to ± 1 mm. Likewise, the maximum angular displacement of the moving-platform allowed for a moment of 0.5 Nm applied on the latter is equal to ± 0.0349 rad ($\pm 2^\circ$).

Twelve points P_j, $j = 1, \ldots, 12$, are selected through the regular workspace of the MEPaM, as shown in Fig. 12, to check whether the constraints related to the maximum point and angular displacements of the moving platform are satisfied or not. The Cartesian coordinates $\mathbf{p}_j$ of points P_j, $j = 1, \ldots, 12$ are the

following:

$$
\begin{aligned}
\mathbf{p}_1 &= \begin{bmatrix} 0 & 0 & z_1 \end{bmatrix}^T \\
\mathbf{p}_2 &= \begin{bmatrix} 0 & r_w & z_1 \end{bmatrix}^T \\
\mathbf{p}_3 &= \begin{bmatrix} r_w\cos\gamma_1 & r_w\sin\gamma_1 & z_1 \end{bmatrix}^T \\
\mathbf{p}_4 &= \begin{bmatrix} r_w\cos\gamma_2 & r_w\sin\gamma_2 & z_1 \end{bmatrix}^T \\
\mathbf{p}_5 &= \begin{bmatrix} 0 & 0 & z_2 \end{bmatrix}^T \\
\mathbf{p}_6 &= \begin{bmatrix} 0 & r_w & z_2 \end{bmatrix}^T \\
\mathbf{p}_7 &= \begin{bmatrix} r_w\cos\gamma_1 & r_w\sin\gamma_1 & z_2 \end{bmatrix}^T \\
\mathbf{p}_8 &= \begin{bmatrix} r_w\cos\gamma_2 & r_w\sin\gamma_2 & z_2 \end{bmatrix}^T \\
\mathbf{p}_9 &= \begin{bmatrix} 0 & 0 & z_3 \end{bmatrix}^T \\
\mathbf{p}_{10} &= \begin{bmatrix} 0 & r_w & z_3 \end{bmatrix}^T \\
\mathbf{p}_{11} &= \begin{bmatrix} r_w\cos\gamma_1 & r_w\sin\gamma_1 & z_3 \end{bmatrix}^T \\
\mathbf{p}_{12} &= \begin{bmatrix} r_w\cos\gamma_2 & r_w\sin\gamma_2 & z_3 \end{bmatrix}^T
\end{aligned}
$$

where the workspace radius r_w is equal to 85 mm and

$$
\begin{aligned}
z_1 &= 0.05 \text{ m} \\
z_2 &= 0.15 \text{ m} \\
z_3 &= 0.25 \text{ m} \\
\gamma_1 &= \pi/6 \text{ rad} \\
\gamma_2 &= -\pi/6 \text{ rad}
\end{aligned}
$$

As a consequence, the following constraints should be satisfied:

$$
\begin{aligned}
\delta p_{xmin} \leq \delta p_{jx} \leq \delta p_{xmax} \quad (11) \\
\delta p_{ymin} \leq \delta p_{jy} \leq \delta p_{ymax} \quad (12) \\
\delta p_{zmin} \leq \delta p_{jz} \leq \delta p_{zmax} \quad (13) \\
\delta\varphi_{xmin} \leq \delta\varphi_{jx} \leq \delta\varphi_{xmax} \quad (14) \\
\delta\varphi_{ymin} \leq \delta\varphi_{jy} \leq \delta\varphi_{ymax} \quad (15) \\
\delta\varphi_{zmin} \leq \delta\varphi_{jz} \leq \delta\varphi_{zmax} \quad (16) \\
j = 1, \ldots, 12 \quad (17)
\end{aligned}
$$

where δp_{jx}, δp_{jy} and δp_{jz} are point-displacements of the moving-platform at point P_j along the x-, y- and z-axes of the base frame $\mathcal{F}_0$, respectively. Likewise, $\delta\varphi_{jx}$, $\delta\varphi_{jy}$ and $\delta\varphi_{jz}$ are the angular displacements of the moving platform at point P_j about the x-, y- and z-axes, respectively. Besides,

$$
\begin{aligned}
\delta p_{xmin} &= \delta p_{ymin} = \delta p_{zmin} = -1 \text{ mm} \\
\delta p_{xmax} &= \delta p_{ymax} = \delta p_{ymax} = 1 \text{ mm} \\
\delta\varphi_{xmin} &= \delta\varphi_{ymin} = \delta\varphi_{ymin} = -0.0349 \text{ rad} \\
\delta\varphi_{xmax} &= \delta\varphi_{ymax} = \delta\varphi_{ymax} = 0.0349 \text{ rad}
\end{aligned}
$$

In order the cross sections of the first two links of each leg to be feasible, the following constraints should be satisfied:

$$
\begin{aligned}
2s_1 \leq b_1 \quad (18) \\
2t_1 \leq h_1 \quad (19) \\
2s_2 \leq b_2 \quad (20) \\
2t_2 \leq h_2 \quad (21)
\end{aligned}
$$

In order the cross sections of the third link of each leg to be feasible, the following constraint should be satisfied:

$$
r_{out} - r_{in} \geq 0.001 \quad (22)
$$

Formulation of the optimization problem

From Eqs.(9) to (22), the optimization problem to be solved takes the form:

$$
\begin{aligned}
\text{minimize } f(\mathbf{x},\mathbf{q}) &= m_{MEPaM} \\
\text{over } \mathbf{x} &= \begin{bmatrix} k_1 & b_1 & h_1 & s_1 & t_1 & k_2 & b_2 & h_2 & s_2 & t_2 & r_{in} & r_{out} \end{bmatrix}^T \\
\text{subject to:} g_1 &: \delta p_{xmin} \leq \delta p_{1x} \leq \delta p_{xmax} \\
g_2 &: \delta p_{ymin} \leq \delta p_{1y} \leq \delta p_{ymax} \\
g_3 &: \delta p_{zmin} \leq \delta p_{1z} \leq \delta p_{zmax} \\
&\vdots \qquad\qquad \vdots \\
g_{34} &: \delta p_{xmin} \leq \delta p_{12x} \leq \delta p_{xmax} \\
g_{35} &: \delta p_{ymin} \leq \delta p_{12y} \leq \delta p_{ymax} \\
g_{36} &: \delta p_{zmin} \leq \delta p_{12z} \leq \delta p_{zmax}
\end{aligned}
$$

$$
\begin{aligned}
&g_{37} : \delta\varphi_{xmin} \leq \delta\varphi_{1x} \leq \delta\varphi_{xmax} \\
&g_{38} : \delta\varphi_{ymin} \leq \delta\varphi_{1y} \leq \delta\varphi_{ymax} \\
&g_{39} : \delta\varphi_{zmin} \leq \delta\varphi_{1z} \leq \delta\varphi_{zmax} \\
&\quad\vdots \qquad\qquad\quad \vdots \\
&g_{70} : \delta\varphi_{xmin} \leq \delta\varphi_{12x} \leq \delta\varphi_{xmax} \\
&g_{71} : \delta\varphi_{ymin} \leq \delta\varphi_{12y} \leq \delta\varphi_{ymax} \\
&g_{72} : \delta\varphi_{zmin} \leq \delta\varphi_{12z} \leq \delta\varphi_{zmax} \\
&g_{73} : 2s_1 \leq b_1 \\
&g_{74} : 2t_1 \leq h_1 \\
&g_{75} : 2s_2 \leq b_2 \\
&g_{76} : 2t_2 \leq h_2 \\
&g_{77} : r_{out} - r_{in} \geq 0.001 \\
&g_{78} : \mathbf{x} \geq \mathbf{x}_{lb} \\
&g_{79} : \mathbf{x} \leq \mathbf{x}_{ub}
\end{aligned} \tag{23}
$$

where vectors $\mathbf{x}_{lb}$ and $\mathbf{x}_{ub}$ contain the lower and upper bounds of the decision variables, namely,

$$
\begin{aligned}
\mathbf{x}_{lb} &= \begin{bmatrix} 1 & 3 & 3 & 0.5 & 0.5 & 1 & 3 & 3 & 0.5 & 0.5 & 0.1 & 2.5 \end{bmatrix}^T \\
\mathbf{x}_{ub} &= \begin{bmatrix} 3 & 100 & 100 & 50 & 50 & 3 & 100 & 100 & 50 & 50 & 10 & 10 \end{bmatrix}^T
\end{aligned}
$$

Vector $\mathbf{q}$ is defined as follows:

$$
\mathbf{q} = \begin{bmatrix} \rho & E & \mu & l_1 & l_2 & r_b & r_p \end{bmatrix}^T \tag{24}
$$

where ρ, E and μ are the density, Young's modulus and Poisson's ratio of the material. l_1 and l_2 are the lengths of links 1 and 2, respectively. r_b and r_p are the base and moving-platform radii, respectively.

Results of the optimisation problem

The optimization problem (23) was solved for the nine pairs of cross section types for links 1 and 2, namely, for the nine sets (k_1, k_2) by means of the *fmincon* Matlab function. Table 2 shows the solutions corresponding to the nine pairs of cross section types. Pair 1-1 has the lowest mass (highlighted in blue in Table 2) and correspond to a MEPaM with both links 1 and 2 having a rectangular hollow cross section. A CAD model is built and shown in Fig. 13. Pair 2-2 has the highest mass (highlighted in red in Table 2) among the nine pairs of cross section types. From the results obtained, it is noteworthy that none of the I-shaped cross sections and H-shaped cross sections converge into rectangular cross sections.

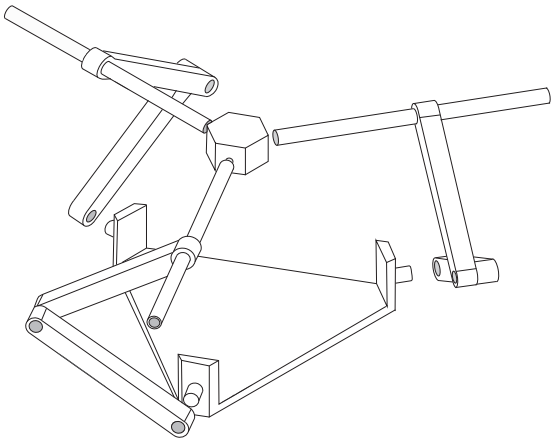

Figure 13. Optimal solution of optimization problem (23)

CONCLUSIONS

This paper dealt with the shape optimization of a six degree-of-freedom haptic interface device, named MEPaM. A regular dexterous workspace was introduced to represent the mobility of user's hand. Throughout this workspace, the deviation of the mobile platform was bounded to provide a better feeling to the user and the masses in motion were minimized to increase the transparency of the haptic device. The stiffness model was written using a virtual joint method and compared with the results obtained with a finite element analysis model.

The shape of the links of the MEPaM were optimized in order to minimize the masses in motion while guaranteeing a given stiffness throughout the regular workspace of the mechanism. Three cross section types were considered for the first two links of each leg of the MEPaM, namely, the rectangular hollow, the I-shaped and the H-shaped cross section types. The third link of each leg had a circular hollow cross section. Therefore, an optimization problem was formulated in order to find the optimal shape and dimensions of each link of the MEPaM that minimize its mass in motion while guaranteeing a given stiffness throughout its regular workspace. The virtual joint method was used to obtain the elasto-static model of the MEPaM with regard to the decision variables and the design parameters of the optimization problem at hand and the manipulator configuration.

Finally, the MEPaM with rectangular hollow cross sections for the first two links of its legs turns to be the optimal solution, namely, the solution that minimizes the mass in motion of the manipulator while satisfying the constraints related to the feasibility of the cross sections and the manipulator's stiffness.

ACKNOWLEDGMENT

The authors would like to acknowledge the financial support of the Egide Programme FAST (FAST Project No 24154WA), the Erasmus Mundus Programme "European Master on Advanced

Table 2. Optimized geometric parameters for different pairs of cross section.

Pair	Link 1					Link 2					Link 3		Mass
	b_1 [m]	h_1 [m]	s_1 [m]	t_1 [m]	k_1	b_2 [m]	h_2 [m]	s_2 [m]	t_2 [m]	k_2	r_{out} [m]	r_{in} [m]	[kg]
1-1	0.0173	0.0166	0.0005	0.0005	1	0.0169	0.0166	0.0005	0.0005	1	0.0057	0.0047	0.3025
1-2	0.0167	0.0190	0.0005	0.0005	1	0.0151	0.0086	0.0029	0.0005	2	0.0063	0.0053	0.4015
1-3	0.0184	0.0174	0.0005	0.0005	1	0.0051	0.0192	0.0005	0.0033	3	0.0060	0.0050	0.3585
2-1	0.0187	0.0086	0.0028	0.0005	2	0.0165	0.0192	0.0005	0.0005	1	0.0063	0.0053	0.4099
2-2	0.0194	0.0100	0.0027	0.0005	2	0.0152	0.0097	0.0029	0.0005	2	0.0068	0.0058	0.5399
2-3	0.0219	0.0088	0.0027	0.0005	2	0.0052	0.0220	0.0005	0.0034	3	0.0065	0.0055	0.4769
3-1	0.0070	0.0210	0.0005	0.0030	3	0.0172	0.0170	0.0005	0.0005	1	0.0058	0.0048	0.3841
3-2	0.0062	0.0272	0.0005	0.0030	3	0.0163	0.0085	0.0029	0.0005	2	0.0065	0.0055	0.4889
3-3	0.0067	0.0225	0.0005	0.0031	3	0.0056	0.0191	0.0005	0.0033	3	0.0061	0.0051	0.4484

ROBotics (EMARO)". Finally, the authors would like to thank Seong Eng CHUAH for his great help.

REFERENCES

[1] Merlet, J., 2006. *Parallel Robots*. Springer, Dordrecht.

[2] Kong, X., and Gosselin, C., 2007. *Type Synthesis of Parallel Mechanisms*. Springer-Verlag, Berlin.

[3] Gogu, G., 2008. *Structural Synthesis of Parallel Robots, Part 1: Methodology*. Springer.

[4] Gogu, G., 2009. *Structural Synthesis of Parallel Robots, Part 2: Translational Topologies with Two and Three Degrees of Freedom*. Springer.

[5] Clavel, R., 1988. "Delta, a fast robot with parallel geometry". In Proceedings of the Int. Symp. On Industrial Robot, pp. 91–100.

[6] Tsai, L., Walsh, G., and Stamper, R., 1996. "Kinematics of a novel three dof translational platform". In Proc. of the 1996 IEEE International Conf. On Robotics and Automation, pp. 3446–3451.

[7] Di Gregorio, R., 2000. "Closed-form solution of the position analysis of the pure translational 3-ruu parallel mechanism". In Proceedings of the 8th Symposium on Mechanisms and Mechanical Transmissions, pp. 119–124.

[8] Gosselin, C., 1993. "On the kinematic design of spherical 3-dof parallel manipulators". *International Jounal of Rohotics Rereach,* ***12***(4), pp. 394–402.

[9] Di Gregorio, R., 2001. "Kinematics of a new spherical parallel manipulator with three equal legs: the 3-urc wrist". *Journal of Robotic Systems,* ***18***(5), pp. 213–219.

[10] Liu, X.J., and Pritschow, G., 2005. "A new family of spatial 3-dof fully-parallel manipulators with high rotational capability". *Mechanism and Machine Theory,* ***40***(4), pp. 475–494.

[11] Liu, X., Wang, J., Wu, C., and Kim, J., 2009. "A new family of spatial 3-dof parallel manipulators with two translational and one rotational dofs". *Robotica,* ***27***(2), pp. 241–247.

[12] Zhao, T., and Huang, Z., 2000. "A novel spatial four-daf parallel mechanism and its position analysis". *Mechonicai Science and Technology,* ***19***(6), pp. 927–929.

[13] Morozov, A., and Angeles, J., 2007. "The mechanical design of a novel schönflies-motion generator". *Robotics and Computer-Integrated Manufacturing,* ***23***(1), pp. 82–93.

[14] Huang, Z., and Li, Q. C., 2002. "General methodology for type synthesis of lower mobility symmetrical parallel manipulators and several novel manipulators". *International Journal of Robotics Research,* ***21***(2), pp. 131–146.

[15] Li, Q., Huang, Z., and Hervé, J., 2004. "Théorie des mécanismes connus sous le nom de parallélogrammes". *IEEE Trans. Robotics and Automation,* ***20***(2), pp. 173–180.

[16] Amine, S., Tale-Masouleh, M., Caro, S., Wenger, P., and Gosselin, C., 2011. "Singularity analysis of 3t2r parallel mechanisms using grassmann-cayley algebra and grassmann line geometry". *Mechanism and Machine Theory*, p. 10.1016/j.mechmachtheory.2011.11.015.

[17] Ben-Horin, P., and Shoham, M., 2006. "Singularity condition of six-degree-of-freedom three-legged parallel robots based on grassmanncayley algebra". *IEEE Transactions on Robotics,* ***22***(4), pp. 577–590.

[18] Dash, A. K., Chen, I.-M., Yeo, S. H., and Yang, G., 2004. "Instantaneous kinematics and singularity analysis of three-legged parallel manipulators". *Robotica,* ***22***(02), pp. 189–203.

[19] Behi, F., 1988. "Kinematic analysis for a six-degree-of-freedom 3-prps parallel mechanism". *IEEE Journal of*

Robotics and Innovation, ***4***(5), pp. 561–565.

[20] Kohli, D., Lee, S., Tsai, K., and Sandor, G., 1988. "Manipulator configurations based on rotary-linear (r-l) actuators and their direct and inverse kinematics". *Journal of Mechanisms, Transmissions, and Automation in Design,* ***110***(4), pp. 397–404.

[21] Cleary, K., and Brooks, T., 1993. "Kinematic analysis of a novel 6-dof parallel manipulator". In IEEE International Conference on Robotics and Automation, pp. 708–713.

[22] Byun, Y., and Cho, H. S., 1997. "Analysis of a novel 6-dof, 3-ppsp parallel manipulator". *The International Journal of Robotics Research,* ***16***(6), pp. 859–872.

[23] Simaan, N., Glozman, D., and Shoham, M., 1998. "Design considerations of new six degrees-of-freedom parallel robots". In IEEE International Conference on Robotics and Automation, pp. 1327–1333.

[24] Lee, S.-U., and Kim, S., 2006. "Analysis and optimal design of a new 6 dof parallel type haptic device". In Intelligent Robots and Systems, 2006 IEEE/RSJ International Conference on, pp. 460 –465.

[25] Caro, S., Moroz, G., Gayral, T., Chablat, D., and Chen, C., 2010. "Singularity analysis of a six-dof parallel manipulator using grassmann-cayley algebra and groebner bases". In Symposium on Brain, Body and Machine, Montreal, QC., Canada.

[26] Chen, C., Gayral, T., Caro, S., Chablat, D., Moroz, G., Abeywardena, S., and Lyons, M., 2011. "A six-dof epicyclic-parallel manipulator". In 15th International Conference on Mechatronics Technology, Melbourne, Australia.

[27] Gosselin, C., and Angeles, J., 1990. "Singularity analysis of closed-loop kinematic chains". *IEEE Trans. on Robotics and Automation,* ***6***, pp. 281–290.

[28] Pashkevich, A., Chablat, D., and Wenger, P., 2009. "Stiffness analysis of overconstrained parallel manipulators". *Mechanism and Machine Theory,* ***44***(5), May, pp. 966–982.

[29] Pashkevich, A., Klimchick, A., and Chablat, D., 2011. "Enhanced stiffness modeling of manipulators with passive joints". *Mechanism and Machine Theory,* ***46***(5), May, p. 662679.

[30] www.haption.com.